Acta Geodyn. Geomater., Vol. 20, No. 4 (212), 179–193, 2023
DOI: 10.13168/AGG.2023.0016
journal homepage: https://www.irsm.cas.cz/acta

ORIGINAL PAPER

ACOUSTIC EMISSION CHARACTERISTICS AND FRACTURE MECHANISM OF GRANITE UNDER THREE-POINT BENDING TEST

Baoshun LIU [1], Chaoqun CHU [1,*] and Qinglong JI [2]

[1] *School of Civil and Resource Engineering, University of Science and Technology Beijing, China*
[2] *Zijin Mining Group Co. Ltd., Longyan, Fujian, China*

**Corresponding author's e-mail:* bkchuchaoqun@163.com

ARTICLE INFO

Article history:
Received 28 September 2023
Accepted 7 December 2023
Available online 21 December 2023

Keywords:
Granite
Three-point bending test
AE
DIC
Moment tensor inversion

ABSTRACT

Due to the influence of various factors such as mineral composition and crystal size, the failure and fracture evolution of granite under three-point bending tests have not been fully determined. In this study, active/passive AE tests are conducted on a cuboid granite specimen at a constant loading rate under a three-point bending test. Acoustic emission monitoring and DIC (Digital Image Correlation) technology are used to investigate the fracture mode and evolution during the fracture process of the specimen. Through analyzing the moment tensor inversion, RA (rise time/amplitude), AF (average frequency) and surface strain field variation characteristics, the fracture characteristics of the specimen is determined. The results show that the fracture of the specimen failure occurs instantaneously. In the early loading stage of the specimen, the main frequency and amplitude of the AE signals are low. However, a large number of high, medium and low frequency AE signals are observed when there is a fracture, which can serve as a precursor to determine the specimen fracture. The fracture type of the specimen is primarily linear tension fracture, with a small proportion of shear fracture, double force couple fracture, and mixed fracture sources. The strain on the surface of the granite specimen is mainly in the X-direction, with a significant increase of proportion in the early stage of fracture. Prior to fracture, the main fracture rapidly propagates from the bottom to the middle of the specimen, leading to the final specimen failure, where it breaks into two distinct blocks along the observable main fracture.

1. INTRODUCTION

In underground engineering excavation in southwestern China, the rock mass is predominantly composed of granite. As the underground excavation goes deeper, the stress on the granite body increases due to excavation and unloading, leading to the concentration of stress in the rock mass. Consequently, micro fractures start to form within the rock mass. The continuous development of micro fractures will cause serious consequences such as rock burst, rock plate peeling, and collapse. When a rock mass undergoes tensile or shear fracture, some of the energy stored inside is released in the form of elastic stress waves, resulting in the phenomenon known as acoustic emission (AE) in the rock. Analyzing the acoustic emission signals with different characteristics and mastering the fracture characteristics during rock failure can provide a technical support for the construction and monitoring in geotechnical engineering.

Due to the widespread occurrence of rock tension fractures in rock engineering and the existence of many bending conditions, the study of rock fracture under bending tests is of great significance. In rock engineering, accurate understanding of the bending strength and modulus of rocks is crucial for the design and stability evaluation of rock structures. The three- point bending test of rocks is an effective means to study the mechanisms of rock fracture and failure, as well as the laws of rock deformation and stress distribution. Peng et al. (2020) conducted semicircular three-point bending tests on four sets of granite specimens treated at different temperatures. The experiments showed that after treatment at 20 ℃-900 ℃, the tensile strength of the rock decreased with the increasing temperature. The temperature range that affected the tensile strength of the rock varied under different fracture modes. Yang et al. (2021) conducted three-point bending tests on four different types of rocks (granite, limestone, marble and sandstone) under a closed pressure of 30 MPa to investigate the initiation and propagation conditions of fractures in specimens under high pressure bending. Qin et al. (2021) used the SonicViewer-SX ultrasonic detection system to detect the rectangular sandstone test under the three-point bending test. Then combined with the evolution of the strain field, deformation field, and energy field of the sandstone sample at the special point of failure, the peak stress and energy field characteristics in different regions of the sample were

obtained. Since Kaiser (1950) discovered the phenomenon of acoustic emission during the observation of metal deformation and summarized the "Kaiser effect", acoustic emission technology has been widely applied in the study of various materials (Cartwright-Taylor et al., 2022; Lockner et al., 1991). Acoustic emission has the advantages of continuity and real-time, which can accurately describe the generation and propagation process of internal cracks in rocks, and locate their failure positions (Lockner, 1993). Through the uniaxial compression tests on pre-damaged granite specimens under high confining pressure cyclic loading, nuclear magnetic resonance (NMR) and acoustic emission were used to analyze the porosity, secondary uniaxial peak strength, and dynamic fracture characteristics of granite before and after the pre-damage test (Zhou and Zhang, 2021). Through the study of high confining pressure loading and unloading tests on granite containing prefabricated fractures, it was believed that AE events were closely related to the deformation, failure, and energy evolution process inside the rock (Gong et al., 2022). Under high confining pressure unloading, the development, aggregation and merging of cracks in granite occur earlier, and there are more high-energy AE events during the failure process. To explore more accurate damage precursors based on multi-acoustic emission indicators, Li et al. (2019) conducted uniaxial loading and unloading tests on granite and marble specimens. It was found that there were almost no AE events in the unloading stage at low stress levels, but more AE events in the unloading stage at high stress levels. It was also proved that the AE count rate can be used as a signal for early warning of rock failure and improved the accuracy of rock dynamic disaster prediction. When studying the development process of micro cracks in sandstone under different high temperatures and stress levels, Sirdesai et al. (2018) divided different stress thresholds and stress states based on the observation results of acoustic emission technology. Since Gilbert (1971) proposed the moment tensor, the moment tensor inversion method has been applied to the study of rock fracture mechanisms. Based on a hybrid iterative algorithm and the jackknife sampling method, Panteleev (2020) reconstructed the seismic moment tensor components of AE events. A new three-stage algorithm was proposed to improve and eliminate the seismic moment tensor solutions of AE events for the granite fracture mechanism under three-point bending tests. Dang et al. (2023) established a three-dimensional model of the failure mechanism of granite after heat treatment using DEM. They quantitatively analyzed the evolution of microcracks and thermal stress of the specimen, and explored the failure mechanism of granite under different heat treatments through moment tensor inversion, obtaining the influence of temperature on the type of seismic source failure. Niu et al. (2022) constructed a set of gas bearing coal load and acoustic emission monitoring experimental system for coal failure under the coupling effect of external stress and gas. The spatial distribution and diffusion trend of AE characteristics before coal failure was analyzed and combined moment tensor inversion method to study the evolution process of coal damage localization. In recent years, digital image correlation (DIC) technology has been combined with AE technology to continuously monitor the studied materials in a non-contact manner. Qin et al. (2022) used DIC technology to quantitatively study the sandstone specimens with unilateral notched beams under three-point bending tests. Combining fracture toughness and peak load, the fracture behavior of sandstone specimens was explained by the changes in the maximum principal strain field and pre-notch pore size. The fracture results of sandstone under different water content and notch offset conditions were analyzed. Sharma et al. (2022) utilized the advantages of AE and DIC non-destructive testing technology to study the bending behavior and fracture mode of reinforced concrete beams reinforced with doped steel and fiberglass. Lacidogna et al. (2021) considered the influence of four-dimensional scale on fracture energy, bending strength and acoustic emission energy per unit area by combining acoustic emission, DIC technology and dynamic identification technology for the formation and propagation of fractures in plain concrete pre-notched beam specimens under three-point bending.

Many achievements have been made in the study of the fracture characteristics, acoustic emission, and surface strain characteristics of granite under three-point bending tests, and this study aims to address two key gaps in the current research: (1) As a common engineering rock, granite often has bending stress during tunnel excavation. However, previous research of granite fracture has primarily focused on the compressive strength of granite, neglecting its flexural strength and failing to comprehensively explore the fracture characteristics of granite; (2) The existing methods for studying tensile fracture in granite are limited and lack comprehensive exploration of the diffusion evolution process of fractures under three-point bending tests combining acoustic emission and the surface strain. Furthermore, these methods failed to systematically describe the deformation characteristics of granite and the relationship between fracture diffusion and acoustic emission characteristics. The process of granite fracture often produces detailed and rapid surface strain changes. How to quickly capture this small change and qualitatively describe the granite fracture process at the micro scale is an urgent problem to be solved. To achieve these research objectives, the study proposes conducting a three-point bending test on a standard rectangular granite specimen. The acoustic emission event information will be recorded using a 12-channel continuous acquisition system of IMaGE and processed using InSite-Lab. Combined with the results of laboratory tests, the failure mode and fracture propagation evolution of the granite

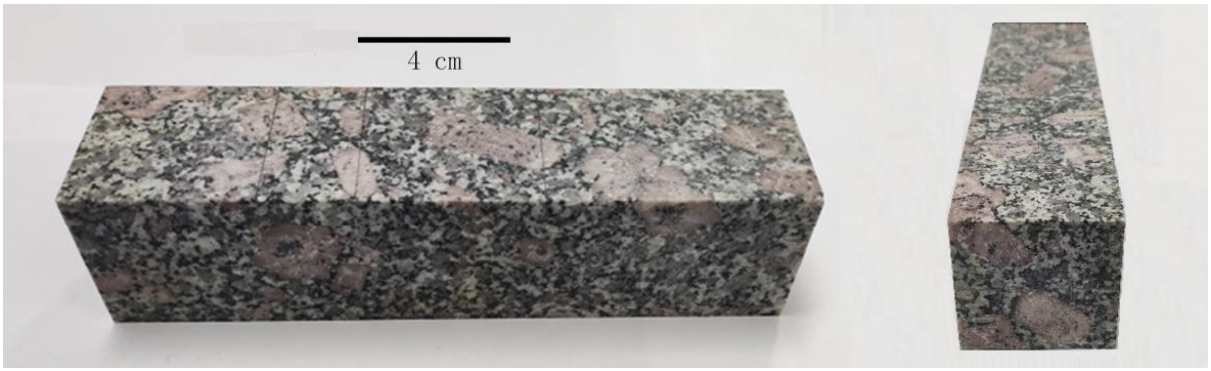

Fig. 1 Front view and left view of the granite specimen.

Table 1 Basic physical and mechanical parameters.

Territorial	Type	Density /(kg·m^{-3})	Uniaxial strength /Mpa	Elastic modulus /GPa	P-wave velocity /(km·s^{-1})
Honghe, Yunnan	Granite	2652.6	143.75	29.85	4.782

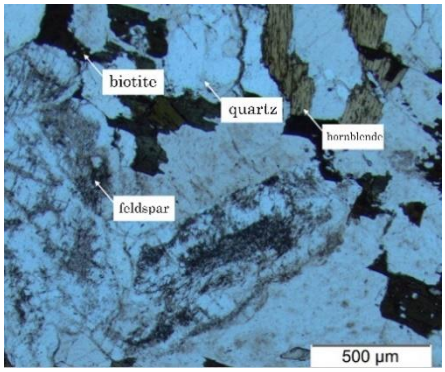

Fig. 2 Orthogonal polarizing microscope photos.

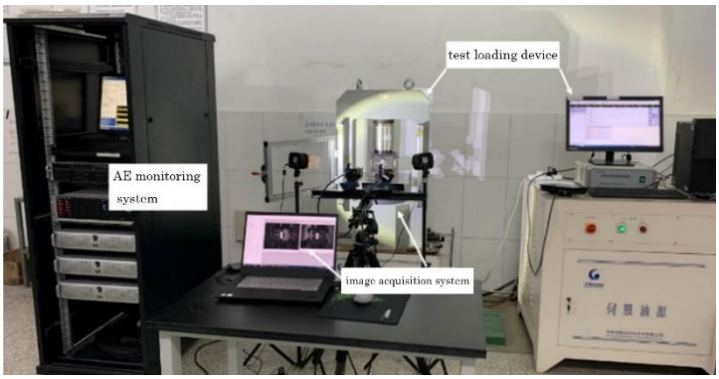

Fig.3 Test equipment and systems.

specimen under three-point bending tests are analyzed based on changes in acoustic emission characteristic parameters. Additionally, the real-time surface strain obtained by DIC technology is combined with the internal fracture types of the specimen to explore the acoustic emission characteristic parameters and surface strain field changes during the fracture process of granite three-point bending. The results can serve as a technical reference for engineering projects involving granite and provide insight into the fracture characteristics of the rock in such conditions.

2. MATERIALS AND METHOD

2.1. GRANITE SPECIMENS

The specimens elected for the three-point bending acoustic emission test was from the borehole core of the Cretaceous granite in the Yanshan period of a highway tunnel in Honghe Prefecture, Yunnan, China. The sampling point was buried at a depth of 900 m. The specimen was cut into a standard cuboid of 200 mm×50 mm×50 mm (length×width×height) recommended by ISRM (the International Society of Rock Mechanics), and then polished smoothly, to ensure that the unevenness of the end face was controlled within ±0.02 mm; the side length error was less than 0.3 mm, and the axis deviation was not more than ±0.25°. The surface of the specimen was checked free of obvious gaps, cracks, delamination, and other defects that may affect the AE experiment and DIC observation (as shown in Fig. 1). The average values of the measured physical and mechanical parameters of the specimen are shown in Table 1. Under the naked eyes, it is composed of gray, white, black and red particles, and the size of mineral particles is mainly 1-3 mm and 10-15 mm, which are embedded in the granite unevenly. The specimen belongs to medium-coarse-grained granite, with unequal grain structure, and block structure. The specimen was randomly taken from the granite to make microscopic slides for optical observation under orthogonal polarizing microscope (as shown in Fig. 2). The specimen has a medium-coarse-grained unequal structure, and its mineral composition mainly includes quartz, feldspar, hornblende and biotite, and most of the minerals are irregularly granular and disorderly distributed.

Table 2 Basic parameters of the acoustic emission monitoring system.

AE components	Types	Parameters
AE acquisition sensor	PICO sensor	Frequency range 200-750 kHz
Signal preamplifier	Pulse amplifier with built-in 100 kHz-1 MHz bandpass filter	Gain range 30-70 dB
AE acquisition system	Richter16 continuous acquisition system	Slaver1, Masterand Slaver2
Pulsed generator	IMaGE equipped with PIU	500 Vpulse
Companion computer	IMaGE equipped with PC	Treatment after eXstream data acquising InSite-Lab

2.2. TEST SYSTEM AND PLAN

(1) Test system

The layout of the test system and equipment are shown in Figure 3. The test loading device adopts YAW-600 microcomputer controlled electro-hydraulic servo rock testing machine, with a maximum loading of 600 KN and a control accuracy of 0.03 μm. The AE system uses the InSite Lab AE monitoring system produced by ASC (Applied Seismology Consultants) in the UK, which has 12 acquisition channels and can excite and record active ultrasonic signals in real-time. The image acquisition system adopts 3D-DIC from Related Solutions

The AE monitoring system includes a high-performance computer that records and processes AE signals, a pulse generator interface unit (PIU) and an amplifier unit (PAD) that actively generates 500 V signals, an AE acquisition system Richter16 composed of three groups of Slaver1, Master, and Slaver2 with 4 channels, eXstream data acquisition software, and InSite-Lab post-processing software. The AE acquisition sensor adopts the PICO sensor from the American Acoustic Physics Company. It has a probe diameter of only 5 mm, whose impact on the AE positioning accuracy is negligible. It's received signal frequency range is 200-750 kHz, with a center frequency of 550 kHz. The signal preamplifier is the core component of the signal-to-noise ratio reduction between the PICO sensor and Richter16, with a built-in pulse amplifier of 100 kHz-1 MHz bandpass filter and an optional gain range of 30-70 dB. When a pulse generator is used to actively excite a 500 V high-voltage pulse during the test, the pre-pulse amplifier can transmit the signal to the PICO sensor to simulate the active wave of the artificial vibrator. The relevant parameters of the AE components are shown in Table 2.

In general, the amplitude of ambient noise in the laboratory does not exceed 30 mV, and the AE events generated by rock fractures can be easily triggered.In the test, the preamplifier gainwas set to 30 mV as the AE threshold, the Trigger Instruments to 3, the Window Length to 480, and the Waveform Length to 1024. When three or more channels record a voltage exceeding 30mV within a length of 480 sampling points, it is considered as triggering one event.

During the test, synchronous active ultrasonic measurements were performed throughout the process. The IMaGE pulse generator used in this experiment can excite pulse signals up to 500 V, which are then transmitted to each PICO sensor through a pre-pulse amplifier, making it the active source for continuous P-wave velocity test. When conducting active ultrasonic testing, 8 sensors located on the surface of the specimen are sequentially used as active sources to emit an ultrasonic signal. At this time, the remaining 7 AE probes are respectively used as passive AE probes to receive this ultrasonic signal.

2) Test plan

The pre-processed standard cuboid specimen was scribed and positioned. Then a 5 mm long fluorine hose was cut, and 502 glue was pasted on the designed sensor point after incision treatment to ensure the fixation of the PICO sensor during the pressurization. The PICO sensor probe was connected to the specimen according to the design number, and the hot melt adhesive was used to fix the smooth side of the PICO sensor probe inside of the fluorine hose using hot melt adhesive. The spray square white matte was painted on the front center of the specimen, and the toner was randomly added to make speckle after the paint was air-dry. Then the specimen was placed in the center of the loading table and connected the high-frequency socket of the PICO sensor probe to the pre-pulse amplifier. When the collected images are calibrated, it is necessary to use the speckle calibration plate to compare and take photos at different locations around the speckle of the specimen for more than 20 groups, and use VIC-3D software for location and calibration. According to the instructions, when the deviation value of the calibration plate in the test results was less than 0.04, it was deemed to be qualified; otherwise, the light needed to be readjusted until it was qualified. The eXstream data acquisition software was used to set the AE sampling frequency to 10 MHz, the waveform digitization resolution to 16 bit, and the preset pulser to send out an active ultrasound wave from each PICO sensor every 70 s after the test load was stable. The VIC-3D data collection software VIC-Snap was used to collect photo data. After the installation and commissioning of the whole system, 400 N was preloaded to ensure that the testing machine and the sample will be in contact with the specimen for voltage stabilization. According to the test settings of rock mechanics specimens on the same testing

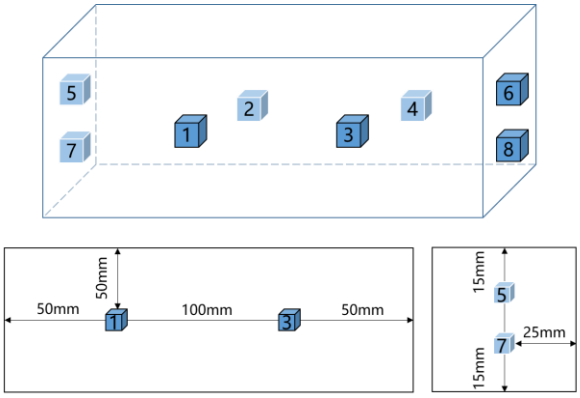

Fig. 4 Schematic diagram of AE sensor distribution.

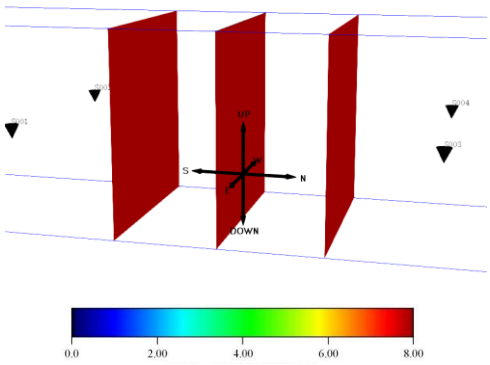

Fig. 5 Density plot of effective sensor number analysis.

machine, the fracture characteristics of granite specimens were combined. The rock testing machine was set to be loaded at a fixed rate of 30 N/s until the specimen was completely damaged (Chu et al., 2023).

3. TEST RESULTS AND ANALYSIS

3.1. ARRAY ANALYSIS

In this test, a total of 8 sensors were designed for active/passive AE signal acquisition and reception, with a central symmetric three-dimensional distribution (as shown in Fig. 4), so as to ensure that there are 2 sensors on each surface parallel to the loading direction, and more than 60 % of the sensor paths pass through the stress concentration area of the specimen. The following analyzes whether the sensor layout is reasonable or not from three aspects:

① Number of effective monitoring sensors. Figure 5 shows the number of effective monitoring sensors that can receive source signals in 3D space in the main failure areas of a simplified model of a granite specimen using shadow space. In this test, the ranges of N (-25 mm+25 mm), E (-25 mm+25 mm), and D (-25 mm+25 mm) observed by DIC are the main failure areas of the specimen. From Figure 5, it can be seen that the 8 sensors can receive all the AE signals in the main failure area.

② Analysis of the sensitivity for positioning earthquake magnitudes. Assuming that all sensors have equal noise thresholds, the InSite Lab software can determine the amplitude of the minimum detectable positioning magnitude by comparing the noise floor with the velocity spectral values at the dominant frequency for a given AE sensor distance, the mean attenuation factor (Q factor) of the medium, the noise level and density. From Figure 6, it can be seen that the minimum detectable source intensity is between -5.14 and -4.29 under the condition of sensor placement in this test. Therefore, this placement plan can monitor almost all AE signals generated in indoor tests.

③ Positioning residual analysis

According to the propagation time and source vector difference of the AE event, the positioning residual space (Misfit Space) is calculated using the norms L1 or L2. In this test, the assumed arbitrary AE event is the center position of the specimen. It can be intuitively seen from Figure 7 that the layout of the sensor scheme in this test realizes the full envelope of the positioning space, and the positioning error within the main failure area is basically within 5×10^{-6} m. The maximum positioning error generated by the sensor with the farthest distance from the assumed AE events

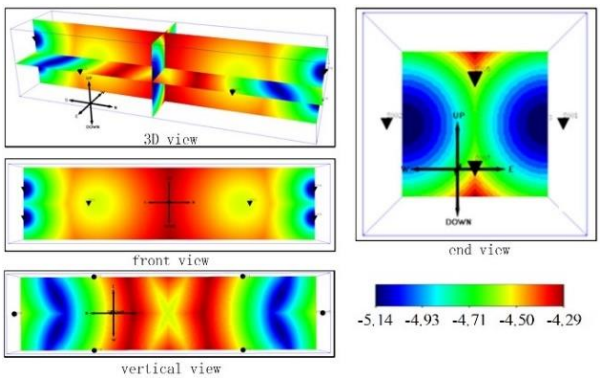

Fig. 6 Density plot of magnitude sensitivity analysis.

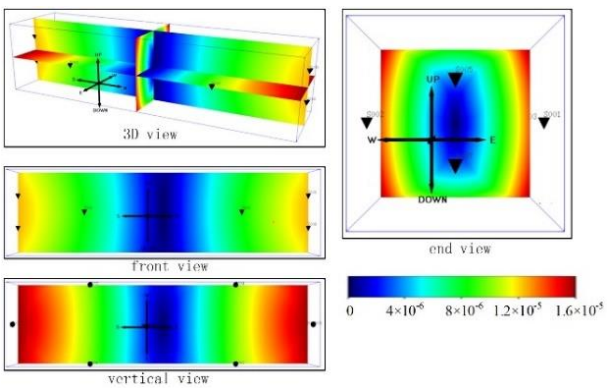

Fig. 7 Color density for location residual analysis.

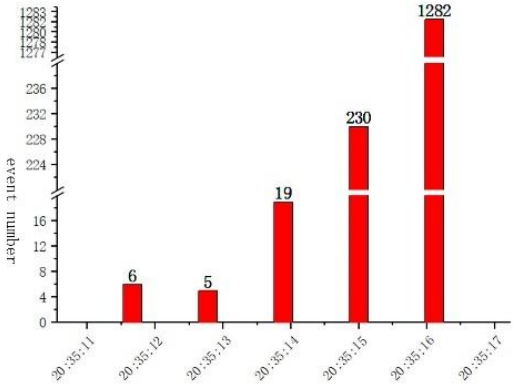

Fig. 8 Distribution graph of load-end events.

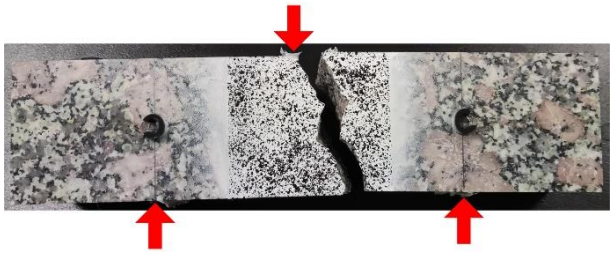

Fig. 9 Fracture results of granite specimens.

is 1.2×10^{-5} m, which meets the test accuracy requirements, but the error is slightly larger. This may be the limitation of the size of the selected specimen, resulting in a 4-fold difference in the distance between the AE sensors in the front-back and left-right (E-W, N-S) directions of the cuboid specimen. However, considering that the positioning of AE sources can select different positioning methods screen AE signal channels, it is believed that the positioning residual results generated by the arrangement of the AE probe array used in this test are better, which meets the requirements of AE monitoring and subsequent AE source positioning.

3.2. ANALYSIS OF AE CHARACTERISTICS OF GRANITE UNDER THREE-POINT BENDING CONDITIONS

According to theabove settings, using IMaGE's AE post-processing software InSite Lab, a total of 1573 high-quality AE events were obtained after the 9-minute AE information recorded in the three-point bending test of granitewas triggered. Almost no AE events were recorded at the beginning of the loading of the granite three-point bending test, and then the AE events were sporadic but only a small number of ringing counts were generated. The AE event burst reached a maximum at the end of the loading (Fig. 8), and then the granite specimen fractured and failed (Fig. 9). The results of the AE tests indicate that granite, as a typical hard and brittle rock specimen, only produces fewer fractures in the early stage of loading. When theenergy accumulated to the limit of bearing capacity, the specimen suddenly fractured, and the AE events increased sharply before the fracture.

The AE signals generated during rock fracture process are discrete and non-stationary and their frequencies vary with time. FFT (Fourier transform) is suitable for processing such signals. The spectrogram of the waveform after FFT transformation of the AE signals at different loading stages of the selected specimen is shown in Figure 10.

Analyzing the spectrogram of the entire AE signal, the main frequency and amplitude of the AE signal are low when the load is just loaded. As the load increases, the amplitude gradually increases, and the amplitude jumps significantly at the end of the loading. The energy is released sharply at the moment when the rock is about to break and the amplitude reaches the highest in the moment before the fracture. The three-dimensional characteristic evolution diagram of main frequency-time-amplitude can visually show the difference between the time distribution characteristics and fracture types of AE events. To further analyze the AE types during the loading process of granite three-point bending tests, the AE events are divided into four stages according to the order in which they occur, as shown in Figure 11: interval A is the calm zone containing events 1-400; interval B is the pre-rupture period containing events 401-800; interval C is the rupture period containing events 801-1200, and interval D is the late fracture containing events 1201-1753. It can be seen from Figure 11 that in the stable period of the loading process of the granite three-point bending tests, the AE events are basically maintained in a high-frequency and low-amplitude state. A small number of low-frequency, low-amplitude and high-frequency medium-amplitude signals may be generated by the closure or expansion of the primary-fractures in the granite. During the calm period before the fracture, the AE events are basically maintained in a high-frequency and low-amplitude state throughout the whole process, which is a typical stress concentrated energy compression behavior before the fracture of brittle and hard rock. During the fracture period, the amplitude of the AE events increases dramatically, and a large number of high-amplitude events indicate that the formation of a large number of fractures and the occurrence of severe damage. Therefore, the main fracture of granite is developed and formed at this stage, and the internal stress concentration is released instantaneously and the rock is fractured. In the later stage of the fracture,

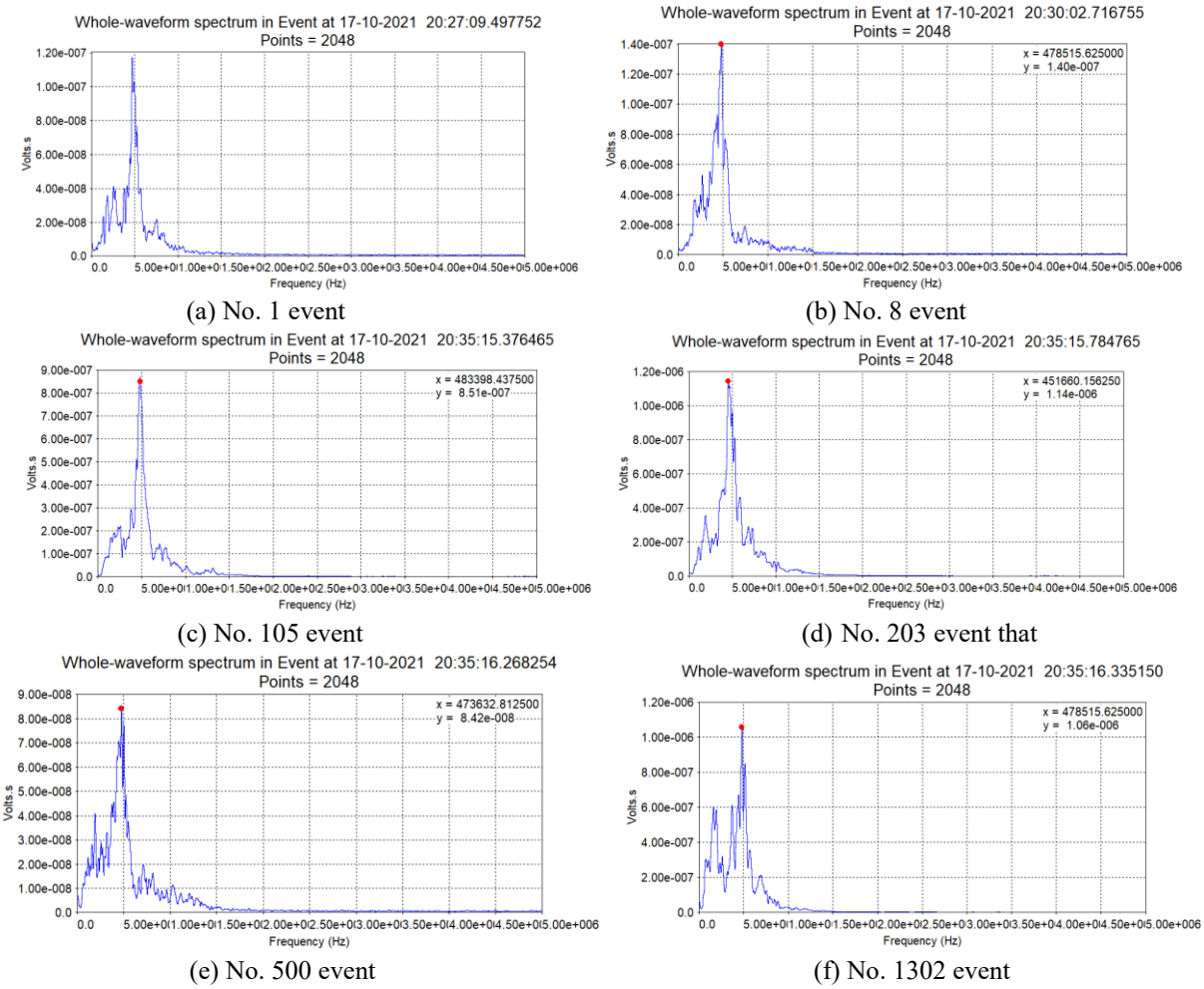

Fig. 10 AE waveform spectrum of granite at different loading stages.

a large number of low-frequency events occurred, with an average proportion of various AE events. This indicates that the fracture of granite in this stage is complex and rich, and the specimen is completely disconnected.

3.3. STUDY ON THE EVOLUTION OF GRANITE FRACTURE UNDER PRIMARY ULTRASOUND TECHNOLOGY

The layout of AE probes and the ultrasonic paths are shown in Figure 12. After preloading the granite sample, an active P-wave velocity test is conducted first, and then an active ultrasonic test is set every 70 s during the loading process. In theory, there are 28 ray paths on the 8 sensors on the surface around the granite specimen (treating 1-2 and 2-1 as the same paths). The 6 paths: 1-4, 3-2, 5-8, 7-6, 1-2 and 3-4 in Figure12, are selected to discuss the wave velocity.

According to the characteristics of the three-point bending failure surface, the ray paths 1-4 and 3-2 that pass through the front and back faces and the ray paths 5-8 and 7-6 on both sides of the end face are selected to study the change of wave speed in the damage, and the ray paths that do not pass through are selected. The fractured ray paths 1-2 and 3-4 are used to compare the changing characteristics of the wave velocity field near the main damage area during three-point bending damage.

The relationship between the 10 active AE pulses excited during the AE test is extracted by InSite-Lab software, and the P-wave velocities of the above 6 ray paths of interest are selected for analysis. The relationship between the P-wave velocities obtained is shown in Figure 13. Since the first velocity measurement in Figure 13 is a three-point bending test preloaded with 400 N, the active ultrasonic velocimetry at this moment can be regarded as the wave velocity of the granite specimen without load loss. At this time, the measured P-wave velocity can be seen that there is a significant difference in the wave velocity between different paths, thereby there is obvious anisotropy in the granite specimen selected for the test. A few paths produce significant fluctuations, such as paths 7-6 fluctuating significantly between the 6th and 7th speed measurements, and it is inferred that the granite specimen may have a large strain in the horizontal direction at this stage.

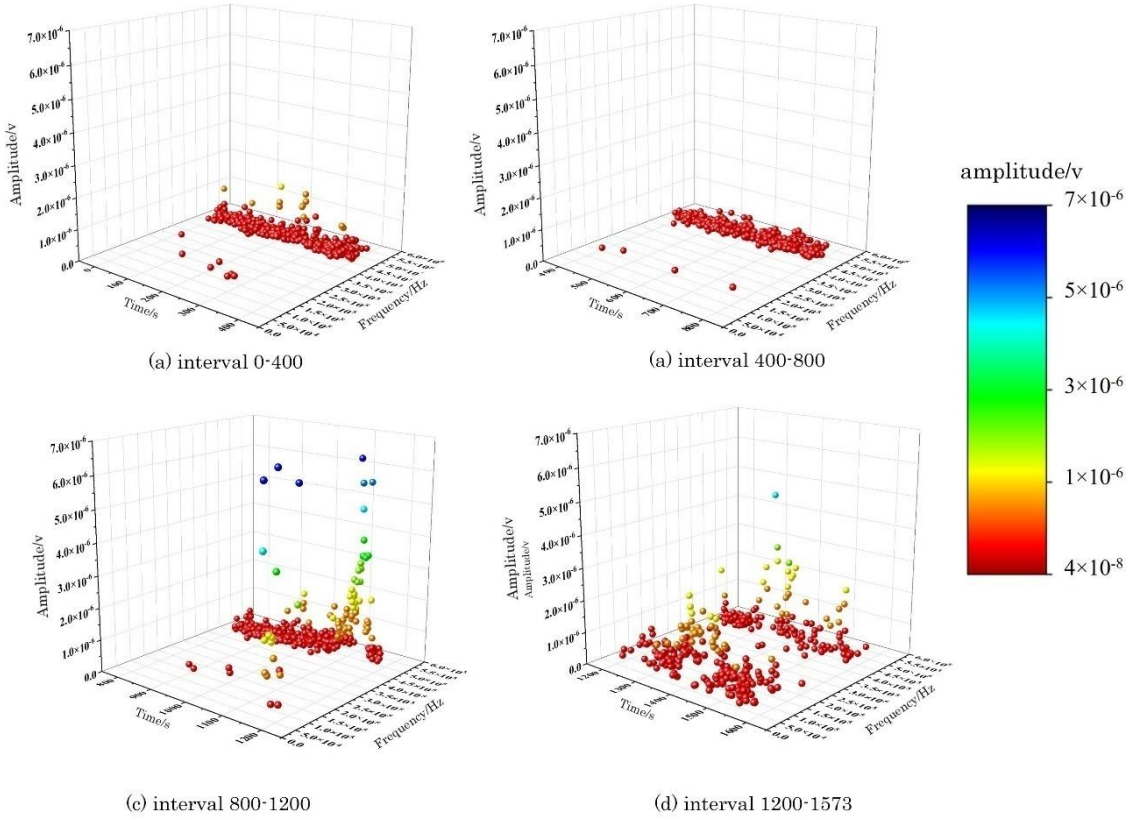

Fig. 11 3D evolution law of main frequency, time and amplitude.

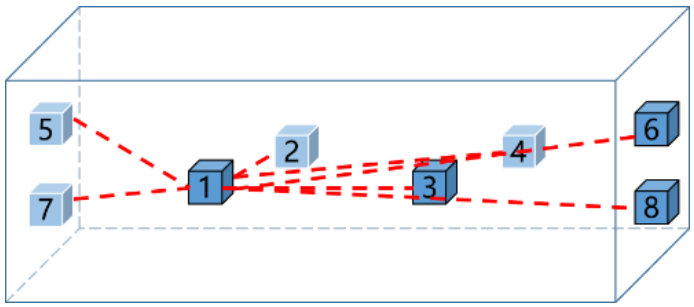

Fig. 12 Schematic diagram of the active ultrasonic propagation path.

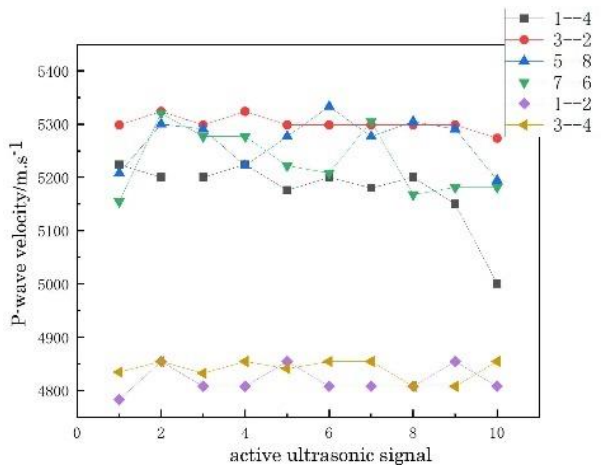

Fig.13 Variation of active ultrasonic wave velocity at different paths.

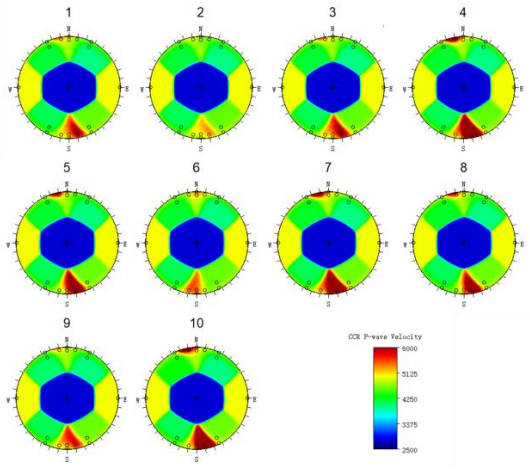

Fig. 14 Hemispheric stereographic projection under wave velocity.

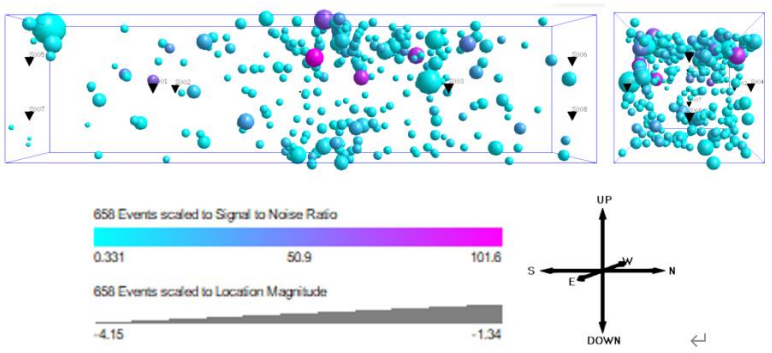

Fig. 15 Location results of AE events.

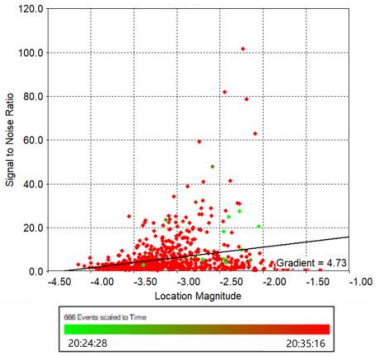

Fig. 16 Correlation between location.

Through the 10 active AE pulses during the specimen process, and combined with CCR (cross-correlation) analysis technology, the waveform collected by the first measurement is selected as the reference waveform to obtain the time difference of the longitudinal wave velocity is obtained. After manual P-wave picking, the waveform collected in the third speed measurement with the best picking effect is selected as the reference waveform. The lower hemisphere chi-flat projection of the P-wave velocity of other ray paths is obtained by CCR analysis (as shown in Fig. 14). It is obtained that the local maximum velocity and minimum velocity of P-wave of the granite cuboid specimen is 5753 m/s and 3375 m/s respectively, with an average velocity of about 4250 m/s, showing significant anisotropy and heterogeneity. Based on the P-wave velocities of different stages, a time-dependent trans isotropic (TTI) velocity model of the cuboid specimen can be constructed (Seifert, 2023), and its P-wave velocity can be expressed as follows:

$$v_{P-r} = \left(\frac{v_2+v_1}{2}\right) - \left(\frac{v_2-v_1}{2}\right)\cos(\pi - 2\theta_r) \quad (1)$$

where $v_{P\text{-}r}$ is the P-wave velocity on the ray path *r* of each pair of source sensors; θ_r is the angle between path r and the axis of symmetry; v_2 is the P-wave phase velocity parallel to the axis of symmetry; v_1 is the P-wave velocity perpendicular to the axis of symmetry, and the relationship between the two is as follows:

$$v_1 = \alpha_A v_2 \quad (2)$$

where α_A is the anisotropy coefficient in the range of [0, 10]. In this three-point bending test, the initial anisotropy coefficient of the specimen is 0.587, indicating that the axis of symmetry is in the direction of fast P-wave.

3.4. ACOUSTIC EMISSION SOURCE LOCATION DURING GRANITE FRACTURE PROCESS

The methods for locating the AE source include the simplex method, the Geiger algorithm and the collapse grid search algorithm. Although the model of the collapse grid search algorithm is the most complex and the slowest to calculate, it is suitable for complex environments with more noise and echo, thereby it is selected to find the location of the source that meets the requirements. In this test, 1573 AE events were successfully triggered, of which 667 were located at the source of the effective AE event with high degree of confidence. From the location magnitude and SNR (signal-to-noise ratio) in the three-dimensional display of the sample model in Figure 15, it can be seen that AE in the granite three-point bending test is mainly concentrated in the middle of the test block. It is relatively evenly distributed near the macroscopic fracture surface, and the events with high SNRs are all located near the main failure area. In this way, it can be concluded that most of the location events have a high degree of confidence (Fig. 16).

The number of AE events observed on the upper surface of the specimen is more than that on the lower surface. To better analyze the facture evolution characteristics under the three-point bending tests, it is necessary to divide the positioning information in more detail. All events are divided into four groups according to the order in which they are triggered: A (1-400), B (401-800), C (801-1200), and D (1201-1573), and the corresponding positioning results of the four groups of events are shown in Figure 17.

Through the analysis of the characteristic parameters of AE, it can be seen that AE events generated by the fracture of the specimen mainly occurs at the moment of fracture. Through analyzing the AE events in groups of 400, it is found that group A almost concentrates the AE events in the whole process of the test. Based on this, it can be seen that the granite fracture is violent and instantaneous in the three-point bending tests. However, from the location results of the AE events, it can be seen that the events are concentrated near the final macroscopic fracture surface of the specimen, which can be considered that the positioning model is more accurate and the positioning results are optimal. In the related studies, the b-value is often used to describe the relationship between the magnitude and frequency of earthquakes.

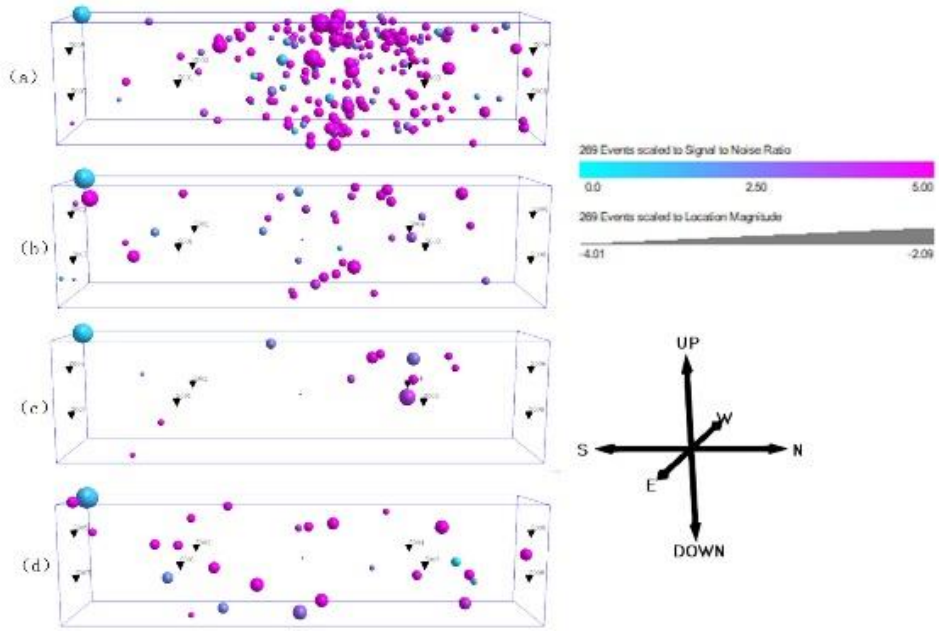

Fig. 17 Localization results of AE events at different stages.

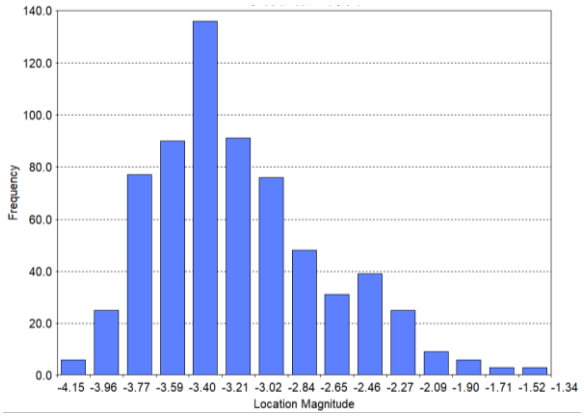

Fig. 18 Location of magnitude distribution.

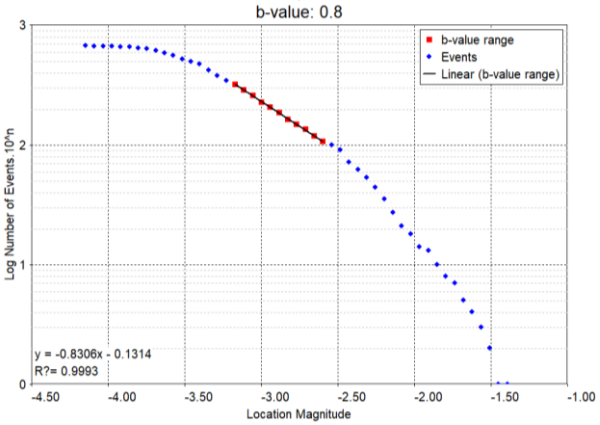

Fig.19 b-value of AE signals.

In AE, its expression means the scale of the magnitude distribution of AE events, that is, the relative number of events with small magnitude and events of large magnitude, expressed as follows:

$$Log_{10}N = a - bM_L \tag{3}$$

where M_L——The location magnitude of AE events; N——The cumulative number of AE events exceeding the location magnitude M_L; a——Constant, obtained by fitting; b——The b-value of AE.

This test only focuses on the relative magnitude distribution, and the analysis uses localized magnitude M_L rather than the true magnitude of AE events. The magnitude distribution of all validly located AE events in Figure18 is fitted to obtain a b-value, grouping the time into each group with a moment magnitude of 0.2. The localized magnitudes of the AE events are mainly distributed between -3.5 and -2.2, and the b-value of AE time obtained by fitting the linear segment is 0.8306 (as shown in Fig.19).

3.5. FRACTURE MECHANISM OF GRANITE BASED ON MOMENT TENSOR INVERSION

The MTI (Moment Tensor Inversion) method is a numerical calculation method used in seismic mechanics for the analysis of earthquake rupture processes. It can invert the mechanical parameters of earthquake fracture process through the analysis of seismic waveform data. The beach sphere plots or T-k plots are commonly used to visualize the results of MTI.AT-k plot is a visualization tool that displays the types of seismic sources, also known as an instantaneous source T-k plot, which is used to describe the longitudinal, transverse, and shear stresses of moment tensors. Hudson defined the moment tensor as two parameters, T and k (Hudson et al., 1989), where T represents the biased component of the moment tensor, and k represents the change of the source volume, thereby measuring the isotropic component of the moment tensor. Using T-k to represent the moment tensor cannot only facilitate the

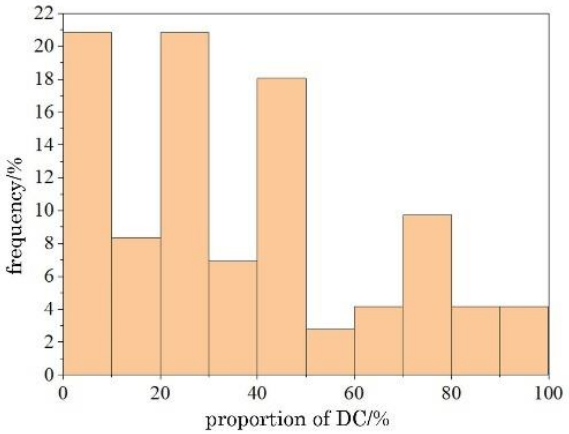

Fig. 20 Statistical histogram of DC component proportion of moment tensor decomposition.

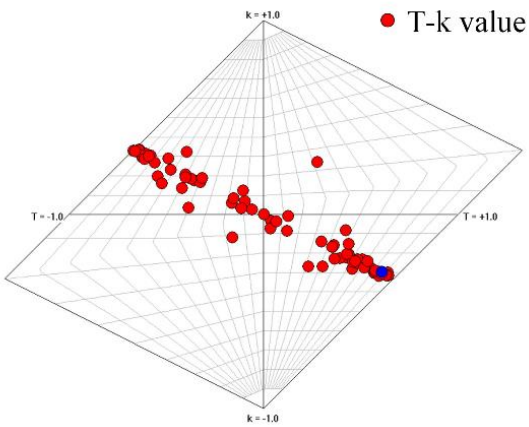

Fig. 21 T-k results of source mechanism.

analysis and calculation of the source mechanism, but also eliminate the dependence on the fracture direction of the sources.

To analyze the fracture mechanism of the specimen source, the moment tensor of the inverted AE event was decomposed into ISO (isotropic parts), DC (pure double couple), and CLVD (compensated linear vector dipole components), and the source events are classified according to the DC component ratio P_{DC} (as shown in Fig. 20). In the whole process of the granite specimen, in the proportion of effective moment tensor decomposition of pure double force couple components in the whole process of AE events of the granite specimen, $P_{DC} \leq 4$ 0 % accounts for 57 %, and $P_{DC} \geq 60$ % accounts for 21 %. The whole process of the granite three-point bending fracture is mainly tensile fracture, which is consistent with the properties of brittle and hard granite. From the T-k diagram of the moment tensor of the AE events (Fig. 21), it can be seen that the source events are mainly concentrated around y=-x/2, with a strong symmetry relationship near the double couple. This case gradually increases and becomes more concentrated in the direction of y=-x/2. The results show that the main fracture of this granite specimen is linear tension fracture, and the proportion of shear fracture, double couple fracture and mixed fracture source is small.

3.6. FRACTURE MECHANISM ANALYSIS BASED ON RA AND AF

The fracture and mode of rock materials are directly related to two indicators: RA (Rise time/Amplitude) and AF (Average Frequency) (Zhang et al., 2023). It is generally believed that a high RA and low AF of the AE signal indicate shear failure of the rock, while a high AF and low RA indicate tensile failure of the rock. Based on the four-step events, the relationship between RA and AF is shown in Figure 22. In the test, the high AF and high RA signals gradually increase as the load increases, while the proportion of high AF and low RA signals in the whole loading process is always high. This indicates that the whole loading process is dominated by tensile fracture, and the closer the fracture stage, the higher the priority of tensile fracture. Based on the results of moment tensor analysis, it can be confirmed that the fracture process of granite is mainly tensile fracture mode.

3.7. THE EVOLUTION OF GRANITE FRACTURE UNDER DIC TECHNOLOGY

When the specimen is loaded until the final test fractures, changes in the specimen surface are difficult to observe with the naked eyes alone. The microscopic deformation is monitored using DIC and VIC-3D software to obtain real-time surface strain and displacement of the granite specimen. The strain of the specimen is obtained by calculating the change in the coordinates of the original region during this process, as shown in Figure 23.

This article studies the changes in the strain field during the failure process of the specimen. The surface of the specimen mainly undergoes displacement and tension. Considering the running speed of the algorithm and other factors, the second-order shape function is selected as the shape function of the DIC calculation.

When using DIC technology to analyze the deformation of the whole process of specimen fracture, the initial calibration image is first imported into the VIC-3D system, so that the camera can be located through calculation in three-dimensional space. Then, the speckle digital images in the whole loading process of the specimen loading are imported, and the deformation area is divided for Lagrangian strain calculation. The change process of the strain field on each image is obtained, which intuitively shows the law of strain evolution and development of the specimen during the loading process. Based on the active ultrasonic velocity measurement event, the

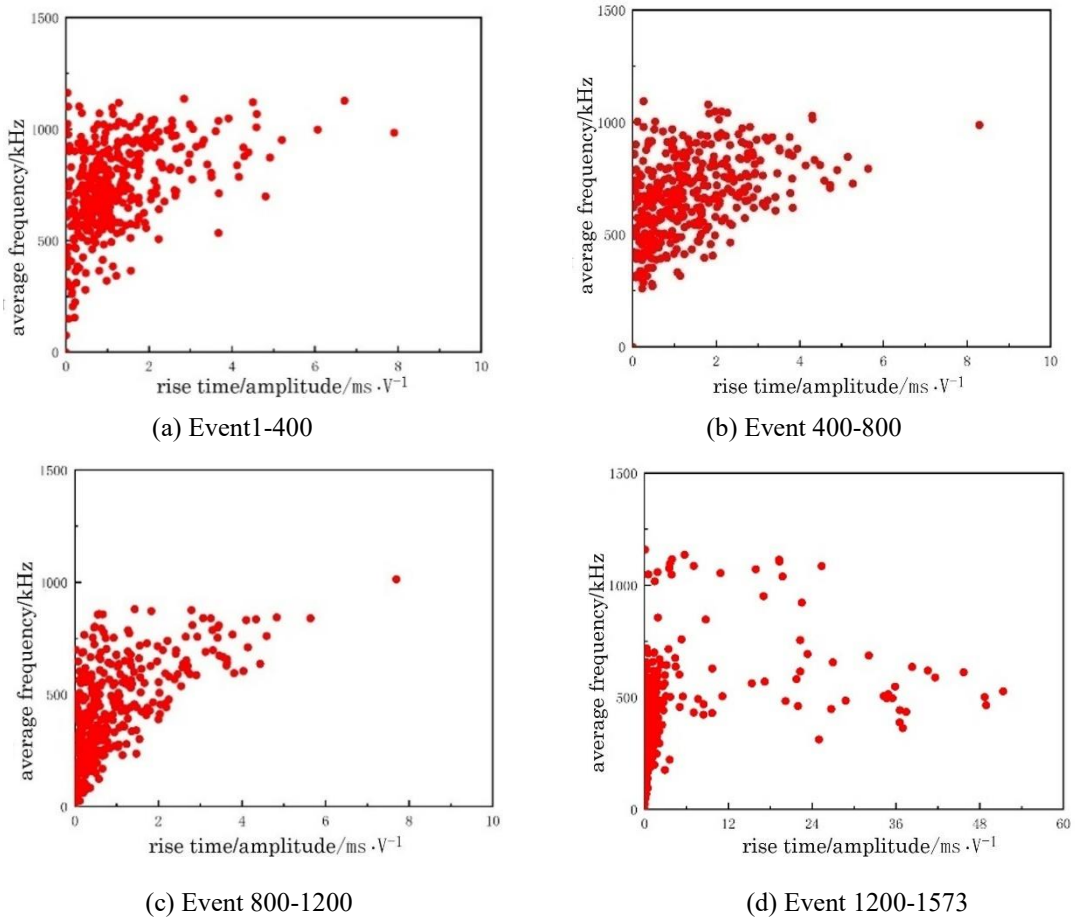

Fig. 22 RA and AF distribution in the four loading stages.

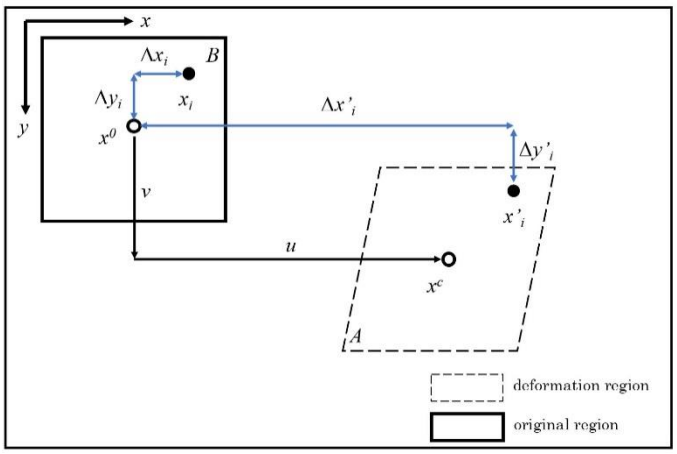

Fig. 23 Schematic diagram of matching deformation areas using digital image correlation technology.

photos in Figures 24, 25 and 26 are taken. The ninth photo shows the results of final failure moment of the specimen. It can be seen that in the first eight active ultrasound velocity measurements, the strain changes on the surface of the sample are not sensitive to the results of active ultrasound. The value of the strain region of the fracture failure in photo (No. IX (580s)) increases significantly. Based on the moment record of the specimen failure, it can be seen that with the loading of the test, the concentration of the force area of the previous specimen is not obvious. Due to the influence of coarse-grained mineral particles of this specimen, the formation of the failure area of the specimen is obviously different from the homogeneous rock, and the fracture begins at the lower right corner of the center of the specimen,

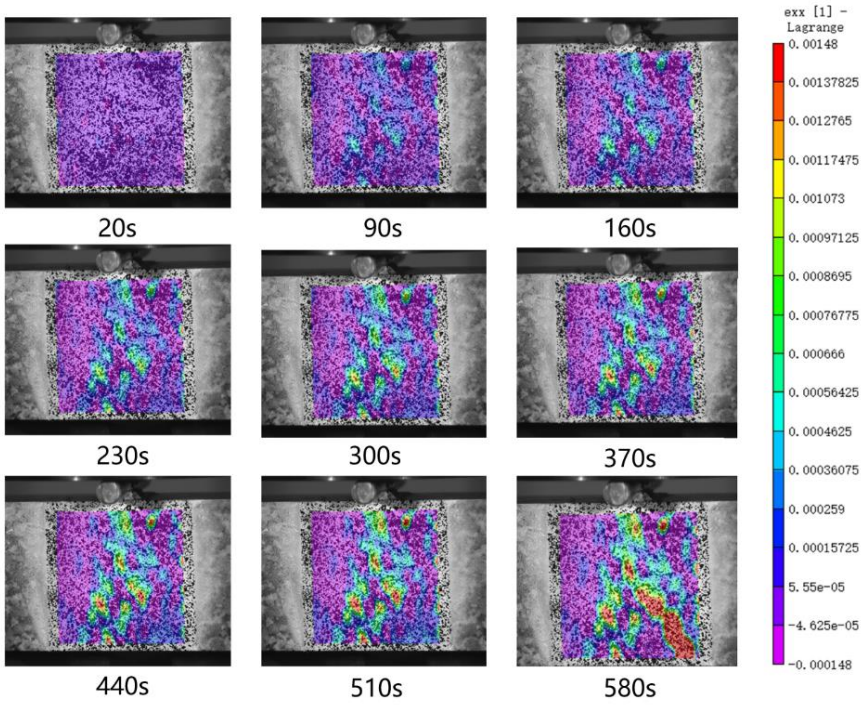

Fig. 24 X-direction strain during granite loading.

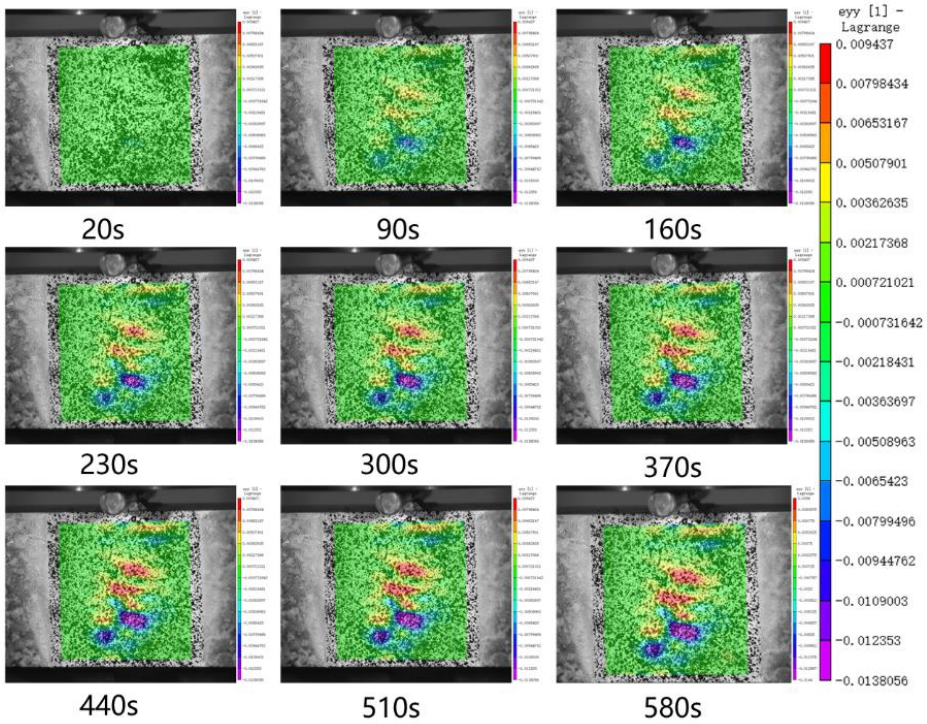

Fig. 25 Y-direction strain during granite loading.

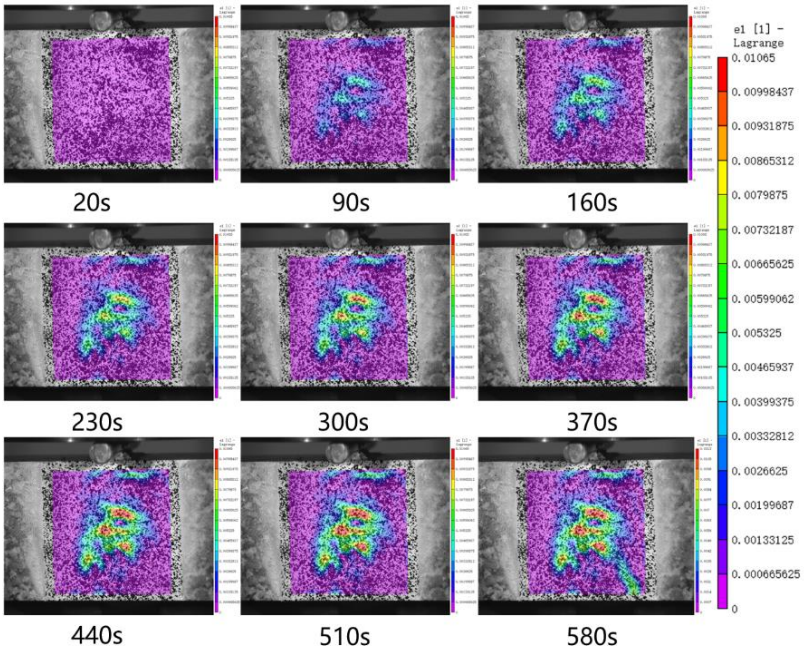

Fig. 26 The main strain during the granite loading.

and the strain value at this position gradually increases. After fracture, the block is intact, and only one main fracture that occurs at the asymmetric axis of the specimen destroys the specimen into two parts.

4. CONCLUSION

Combined with DIC surface strain monitoring technology, active/passive AE monitoring is used to study the three-point characteristics of coarse-grained granite specimen with uneven particles from the aspects of acoustic emission characteristic parameters, wave speed changes, source mechanism analysis, and surface strain field evolution characteristics. The fracture mechanism and precursor information under bending conditions can provide a reference for the analysis and evaluation of rock bending deformation in engineering. The main conclusions are as follows:

(1) Under three-point bending loading test, the specimen failure has instantaneous fracture characteristics, and the whole loading process is dominated by horizontal stress. Final fracture of the specimen is affected by the large internal grain crystals, and the fracture surface of the specimen is not in a left-right symmetrical position.

(2) In the early stage of loading, the main frequency and amplitude of AE are low. In the early stage of fracture, the AE event occurs during the quiet period and is always in a state of high-frequency and low-amplitude throughout the process. At the moment of fracture, a large number of AE signals appear appears, and the frequency band distribution of the main frequency signal becomes wider. Then a large number of high, medium and low frequency signals appear, and various types of AE signals appear, showing changes from high frequency and low amplitude to full frequency band distribution. This phenomenon can be identified as a precursor to fracture.

(3) The analysis of the earthquake failure mechanism reveals an increasing trend in the proportion of tensile fractures in the early stages of fracture. Additionally, the comparison s of results from RA/AF and moment tensor decomposition supports the evidence that the fracture mode in the three-point bending test of granite is tensile fracture.

(4) The use of DIC technology allows for the observation of micro crack evolution in granite. It reveals that the surface strain of granite mainly exhibits in x-direction. In the early stage of fracture, the proportion of x-direction strain increases significantly. Prior to the final fracture, the main fracture rapidly expands from the bottom to the middle of the specimen, ultimately leading to instant specimen fracture. The changes in the surface strain provide a clear indication that the evolution of the x-direction strain is the primary characteristic under three-point bending test. Hence, monitoring efforts should primarily focus on this aspect.

ACKNOWLEDGEMENTS

The work was financially supported by the National Natural Science Foundation of China (No. 51934003).

REFERENCES

Cartwright-Taylor, A., Mangriotis, M.D., Main, I.G., Butler, I.B., Fusseis, F., Ling, M. and Magdysyuk, O.V.: 2022, Seismic events miss important kinematically governed grain scale mechanisms during shear failure of porous rock. Nature Communications, 13(1), 6169. DOI: 10.1038/s41467-022-33855-z

Chu, C., Wu, S., Zhang, C. and Zhang, Y.: 2023, Microscopic damage evolution of anisotropic rocks under indirect tensile conditions: Insights from acoustic emission and digital image correlation techniques. International Journal of Minerals, Metallurgy and Materials, 30, 1680–1691. DOI: 10.1007/s12613-023-2649-y

Dang, Y., Yang, Z. and Liu, X.: 2023, Three-dimensional numerical study on failure mechanism of granite after thermal treatment based on moment tensor inversion. Computers and Geotechnics, 155, 105185. DOI: 10.1016/j.compgeo.2022.105185

Gilbert, F.: 1971, Excitation of the normal modes of the Earth by earthquake sources. Geophysical Journal International, 22(2), 223–226. DOI: 10.1111/j.1365-246X.1971.tb03593.x

Gong, H., Luo, Y., Xu, K., Huang, J., Wang, G. and Li, X.: 2022, Failure behaviors of fractured granite during loading and unloading under high confining pressure based on acoustic emission multi-parameter analysis. Theoretical and Applied Fracture Mechanics, 121, 103442. DOI: 10.1016/j.tafmec.2022.103442

Hudson, J.A., Pearce, R.G. and Rogers, R.M.: 1989, Source type plot for inversion of the moment tensor. Journal of Geophysical Research: Solid Earth, 94(B1), 765–774. DOI: 10.1029/JB094iB01p00765

Kaiser, J.: 1950, Investigations into the occurrence of repeated requests for trains. Doctoral dissertation, Ph. D. Thesis, Technical Hutchshule, Munich.

Lacidogna, G., Piana, G., Accornero, F., and Carpinteri, A.: 2021, Multitechnique damage monitoring: application to concrete beams. Acoustic Emission and Related Non-Destructive Evaluation Techniques in the Fracture Mechanics of Concrete (Second Edition), 281–301. DOI: 10.1016/B978-0-12-822136-5.00014-9

Li, D., Wang, E., Kong, X., Jia, H., Wang, D. and Ali, M.: 2019, Damage precursor of construction rocks under uniaxial cyclic loading tests analyzed by acoustic emission. Construction and Building Materials, 206, 169–178. DOI: 10.1016/j.conbuildmat.2019.02.074

Lockner, D., Byerlee, J. D., Kuksenko, V., Ponomarev, A. and Sidorin, A.: 1991, Quasi-static fault growth and shear fracture energy in granite. Nature, 350, 39–42. DOI: 10.1038/350039a0

Lockner, D.: 1993, The role of acoustic emission in the study of rock fracture. International Journal of Rock Mechanics and Mining Sciences & Geomechanics Abstracts, 30(7), 883–899. DOI: 10.1016/0148-9062(93)90041-B

Niu, Y., Wang, E. and Li, Z.: 2022, A study on moment tensor inversion of acoustic emission response on damaging localization of gas-bearing coal under load. Scientific Reports, 12, 16360. DOI: 10.1038/s41598-022-20603-y

Panteleev, I.A.: 2020, Analysis of the Seismic Moment Tensor of Acoustic Emission: Granite Fracture Micromechanisms During Three-Point Bending. Acoustical Physics, 66, 653–665. DOI: 10.1134/S106377102006007X

Peng, K., Lv, H., Yan, F.Z., Zou, Q.L., Song, X. and Liu, Z.P.: 2020, Effects of temperature on mechanical properties of granite under different fracture modes. Engineering Fracture Mechanics, 226, 106838. DOI: 10.1016/j.engfracmech.2019.106838

Qin, T., Ren, K., Liu, Z., Duan, Y. and Wang, L.: 2021, Mechanical Characteristics and Energy Evolution of Sandstone Three-Point Bending Test. Shock and Vibration, 2021, 8443777. DOI: 10.1155/2021/8443777.

Qin, X., Su, H., Feng, Y., Zhao, H. and Pham, T.N.: 2022, Fracture and deformation behaviors of saturated and dried single-edge notched beam sandstones under three-point bending based on DIC. Theoretical and Applied Fracture Mechanics, 117, 103204. DOI: 10.1016/j.tafmec.2021.103204

Seifert, T.: 2023, Time-dependent and Time-independent Models of Cyclic Plasticity for Low-cycle and Thermomechanical Fatigue Life Assessment. In: Altenbach, H., Ganczarski, A. (eds) Advanced Theories for Deformation, Damage and Failure in Materials. CISM International Centre for Mechanical Sciences, Springer, Cham, 605, 177–234. DOI: 10.1007/978-3-031-04354-3_4

Sharma, G., Sharma, S. and Sharma, S.K.: 2022, Monitoring structural behaviour of concrete beams reinforced with steel and GFRP bars using acoustic emission and digital image correlation techniques. Structure and Infrastructure Engineering, 18(2), 167–182. DOI: 10.1080/15732479.2020.1836661

Sirdesai, N.N., Gupta, T., Singh, T.N. and Ranjith, P.G.: 2018, Studying the acoustic emission response of an Indian monumental sandstone under varying temperatures and strains. Construction and Building Materials, 168, 346–361. DOI: 10.1016/j.conbuildmat.2018.02.180

Yang, H, Krause, M. and Renner, J.: 2021, Determination of Fracture Toughness of Mode I Fractures from Three-Point Bending Tests at Elevated Confining Pressures. Rock Mechanics and Rock Engineering, 54(10), 5295–5317. DOI: 10.1007/S00603-021-02432-Z.

Zhang, C., Feng, Z., Mi, C., Chen, Z., Geng, H. and Shen, C.: 2023, Experimental study on acoustic emission characteristics of high temperature thermal shock directional fracturing of granite with different heating conditions. Engineering Fracture Mechanics, 289, 109427. DOI: 10.1016/j.engfracmech.2023.109427

Zhou, X. and Zhang, J.: 2021, Damage progression and acoustic emission in brittle failure of granite and sandstone. International Journal of Rock Mechanics and Mining Sciences, 143, 104789. DOI: 10.1016/j.ijrmms.2021.104789